Applied Catalysis B: Environmental 246 (2019) 330–336

Contents lists available at ScienceDirect

Applied Catalysis B: Environmental

journal homepage: www.elsevier.com/locate/apcatb

Insight into iron group transition metal phosphides (Fe_2P, Co_2P, Ni_2P) for improving photocatalytic hydrogen generation

Zhichao Sun[a,b], Mingshan Zhu[c,*], Xingshuai Lv[d], Yingya Liu[a,b], Chuan Shi[a], Ying Dai[d,*], Anjie Wang[a,b,*], Tetsuro Majima[e]

[a] State Key Laboratory of Fine Chemicals, Dalian University of Technology, Dalian, 116024, PR China
[b] Liaoning Key Laboratory of Petrochemical Technology and Equipments, Dalian University of Technology, Dalian, 116024, PR China
[c] Guangdong Key Laboratory of Environmental Pollution and Health, School of Environment, Jinan University, Guangzhou, 510632, PR China
[d] School of Physics, Shandong University, Jinan, 250100, PR China
[e] The Institute of Scientific and Industrial Research (SANKEN), Osaka University, Mihogaoka 8-1, Ibaraki, Osaka, 567-0047, Japan

ARTICLE INFO

Keywords:
Metal phosphides
Sulfur doped g-C_3N_4
Noble metal-free
Photocatalysis
Hydrogen generation

ABSTRACT

Iron group transition metal phosphides (TMPs, M= Fe, Co, Ni) have been considered as promising noble-metal-free cocatalysts for the photocatalytic hydrogen (H_2) generation. However, the impact on the H_2 generation activity in correlation with the types of metal in TMPs still remains unresolved. In this paper, to investigate the effect of metal phosphides with different metal on photocatalytic H_2 generation, three types of iron group transition metal phosphides (M_2P, M = Fe, Co, and Ni) nanoparticles were used as the cocatalysts of sulfur doped g-C_3N_4 (S−CN) for the photocatalytic H_2 generation. By comparing three types of M_2P/S−CN, the optimum cocatalyst of Ni_2P has *ca.* 22.7 times that of the pristine S−CN under the same condition. The photoluminescence (PL) spectra, photoelectrochemical characterization and DFT calculations confirmed the enhanced photo-induced charge transfer and band separation when S−CN was integrated with the Ni_2P.

1. Introduction

Transition metal phosphides (TMPs) which are composed of low-cost and earth-abundant elements, are extensively applied to metallurgy [1], hydrotreating [2,3], pesticides, and gradually used into electrocatalysis [4], lithium ion batteries [5], photocatalysis [6] in recent years. As early as 2005, Rodriguez and co-workers predicted that Ni_2P could be act as a promising alternative to Pt for using in the hydrogen evolution reaction process based on density functional theory (DFT) calculations [7]. The experiment verified this prediction that Ni_2P was definitely an efficient hydrogen evolution reaction catalyst in acidic system until 2013 [8]. Until now, there are six transition metals (Ni, Co, Mo, Fe, Cu and W) that are developed to form TMPs which could act as efficient electrocatalysts [9]. In photocatalytic water splitting progress, TMPs have been used as cocatalysts to separate photo-induced electron-hole pairs and lower the overpotential on the surface of semiconductors [10].

Among these transition metal phosphides, iron group transition metal phosphides such as Fe_2P, FeP, Co_2P, CoP, Ni_3P, Ni_2P, etc., have shown excellent photocatalytic H_2 generation activity as a cocatalyst [11–15]. However, most of the researches were focus on single TMPs hybrid with the suitable semiconductor, such as CoP hybrid with fluorescein-based dye [16], CdS [17], and g-C_3N_4 [18] or Ni_2P hybrid with CdS [19], g-C_3N_4 [20]. Moreover, some reports have related to a series of TMPs with the same metal. For example, Liu's group investigated the difference between Co_2P, CoP, and cobalt phosphide based materials as an efficient electrocatalysts [21]. We also reported that a series of nickel phosphide with different nickel phosphorus ratio acts as a cocatalyst combine with g-C_3N_4 for excellent H_2 generation under visible light [22]. The results demonstrated that the content of phosphorus atoms in the TMPs play important roles for H_2 generation due to its higher electronegativity which can draw electrons from metal atoms [22,23]. In addition to this, overpotential, electronic transmission capacity, stability, and many other factors could impact the H_2 generation activity as well, which could be altered by the type of metal in the TMPs [24].

However, limited research has assessed the impact on the H_2 generation activity in correlation with different types of metal in iron group TMPs. This may due to, on the one hand, the preparation methods of TMPs for different metals are generally different which makes the result lack of comparison [25,26]. On the other hand, how to analyze the effect of different metals phosphide as a photocatalytic cocatalyst and

* Corresponding authors.
E-mail addresses: mingshanzhu@yahoo.com (M. Zhu), daiy60@sina.com (Y. Dai), ajwang@dlut.edu.cn (A. Wang).

https://doi.org/10.1016/j.apcatb.2019.01.072
Received 14 November 2018; Received in revised form 18 January 2019; Accepted 27 January 2019
Available online 29 January 2019
0926-3373/

the influence of photocatalytic hydrogen generation still need to be solved. In this paper, three typical iron group transition metal phosphides (M_2P), Fe_2P, Co_2P, and Ni_2P with the same metal phosphorus ratio were prepared by H_2 plasma reduction (PR) method under mild condition. Based on the characterization techniques, all the different types of M_2P exhibit the similar particle size and crystallization. Furthermore, we chose sulfur doped g-C_3N_4 (S—CN) as a photocatalyst and decorated it with M_2P as a cocatalyst to investigate the photocatalytic hydrogen generation performance under the visible light irradiation. By means of first-principles DFT calculations, Ni_2P hybrid with S—CN exhibits the most suitable activity due to the suitable H* adsorption and the lowest overpotential, which lead to the most effective charge separation ability and the highest H_2 generation activity under visible light irradiation.

2. Experimental

2.1. Chemicals

Iron nitrate hexahydrate ($Fe(NO_3)_2{\cdot}6H_2O$), Cobalt nitrate hexahydrate ($Co(NO_3)_2{\cdot}6H_2O$), Nickel nitrate hexahydrate ($Ni(NO_3)_2{\cdot}6H_2O$), Ammonium phosphate ($(NH_4)_2HPO_4$), urea, thiourea (H_2NCSNH_2), N,*N*-dimethylformamide (DMF), triethanolamine (TEOA) and ethanol were obtained from Sinopharm Chemical Reagent Co. Ltd. (China). $H_2PtCl_6{\cdot}6H_2O$ was provided by J&K Company. All chemicals (AR grade) were of analytical grade and used without further purification. The water used in this study was deionized and purified through a water purification system (resistivity: ˜18 MΩ·cm).

2.2. Preparation of Fe_2P, Co_2P, and Ni_2P

The oxide precursors with metal/P atomic ratio of 2 were synthesized by co-precipitation from metal nitrate and $(NH_4)_2HPO_4$, followed by calcination in air at 773 K for 2 h. The synthesis of M_2P was performed in a dielectric barrier discharge (DBD) reactor [27], which was composed of a quartz tube and two electrodes (Scheme S1). The voltage of the high-voltage electrode was maintained at around 8, 9, and 7 kV for 2 h for Fe_2P, Co_2P, and Ni_2P, respectively. The obtained M_2P were passivated with 0.5%O_2/He before use. As-prepared Fe_2P, Co_2P, and Ni_2P are collectively referred to as M_2P (M = Fe, Co, and Ni).

2.3. Preparation of S-CN

10 g thiourea was placed into a porcelain crucible with a cover, then calcined at 793 K for 2 h in air at a ramp rate of 5 K· min^{-1}. The obtained solid residue was strongly grinded in the agate mortar to make sure the formation of fine powder. The yellow outcome was sulfur doped g-C_3N_4 and was signed as S-CN [28].

2.4. Preparation of M_2P/S-CN

In a typical process, 95 mg S-CN was suspended in 20 mL DMF and kept under ultrasound for 30 min. Then 5 mg of M_2P was added into the suspension liquid under ultrasound for 1 h, then stirred for another 12 h. The resultant was centrifuged, and washed with water, ethanol, then dried at 323 K. The production was marked as M_2P/S-CN and the loading amount of M_2P was 5 wt%.

2.5. Characterization

The crystalline structures of as-prepared samples were characterized by X-ray diffraction (XRD, Rigaku D/Max 2400 diffractometer with nickel-filtered Cu-Kα radiation at 40 kV and 100 mA). Chemical compositions of the samples were examined by X-ray photoelectron spectroscopy (Multilab 2000 X-ray photoelectron spectrometer, using an Mg-Kα source). TEM, HRTEM and scanning TEM (STEM)-EDX elemental mapping were achieved by a FEI Tecnai G2 F30 transmission microscope operated at 300 kV. The UV–vis absorption and diffuse reflectance spectra were measured by JASCO UV-550 spectrophotometer. Elemental analysis was carried out by means of Inductively Coupled Plasma Optical Emission Spectroscopy (ICP-OES). Total specific surface area was measured on Tristar II 3020 and calculated according to the Brumauer–Emmett–Teller (BET) methods. Room temperature photoluminescence (PL) spectra were measured with a Hitachi FL-4500 fluorescence spectrometer. Fluorescence decay spectra were gained by a FluoroMax-4 P spectrophotometer. The photoelectrochemical measurements were recorded on a BAS-100 W electrochemical potentiostat in a three-electrode cell.

2.6. Photocatalytic H_2 generation

For a typical photocatalytic H_2 generation test, 2 mg of photocatalyst was suspended in 5 mL of aqueous solution containing 10 vol% TEOA. Then the sample was sealed and purged with Argon for 30 min to remove air before irradiation. The sample tube was irradiated with a Xe light source (CEL-PF300-T8, Beijing China Education Au-light Co., Ltd) with constant magnetic stirring at room temperature. The evolved gases were analyzed by gas chromatography (Agilent 7890) equipped with a thermal conductive detector (TCD) and a 5 Å molecular sieve column. Wavelength dependence of the H_2 generation rate was detected by using an appropriate band pass filter (400, 440, 480, or 520 nm).

3. Results and discussion

The crystalline structure and the purity of as-synthesized M_2P were characterized by XRD (Fig. S1). The diffraction peaks of Fe_2P at 40.2°, 44.2°, 47.3°, 52.9°, 54.1°, 54.6°, 73.7°, and 79.1° can be indexed as a hexagonal Fe_2P with the JCPDS card file no. 85-1727. The pattern of Co_2P exhibited diffraction peaks at 40.7°, 41.0°, 42.0°, 43.3°, 44.1°, 48.7°, 50.4°, 51.5°, 52.0°, and 56.2°, to be assigned to an orthorhombic Co_2P (JCPDS 65–2380). For Ni_2P, the diffraction peaks present at 40.7°, 44.6°, 47.4°, 54.2°, 55.0°, and 74.8°, which exhibited the similar diffraction peaks of Fe_2P, are corresponded to the structure of Ni_2P (JCPDS 74–1385). This may due to Ni_2P and Fe_2P both adopt the same hexagonal structure. The above XRD patterns indicated the successful formation of the desired phase of Fe_2P, Co_2P, and Ni_2P with our synthetic method. The XRD patterns of S-CN and the pristine M_2P hybrid with S-CN were observed to show the formation of M_2P/S-CN composite materials, as shown in Fig. 1. The high-angle peak at 27.4° was detected in pristine S-CN, assigned to an interlayer stacking of conjugated aromatics [4]. The hybrid samples exhibit the characteristic diffraction peaks of both M_2P and S-CN, indicating that the structure of M_2P and S-CN both remained after hybridization. The weak diffraction intensities of M_2P phase corresponds to the low weight ratio in the

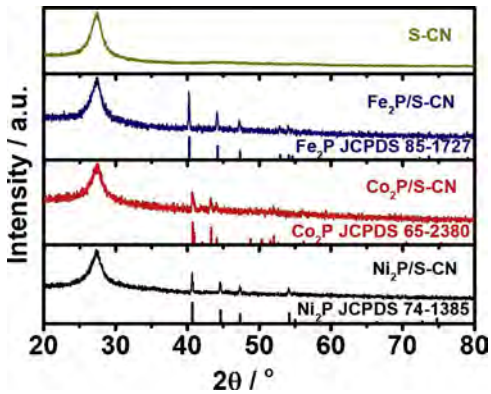

Fig. 1. XRD patterns of as-prepared S-CN, Fe_2P/S-CN, Co_2P/S-CN, Ni_2P/S-CN, and corresponding standard PDFs.

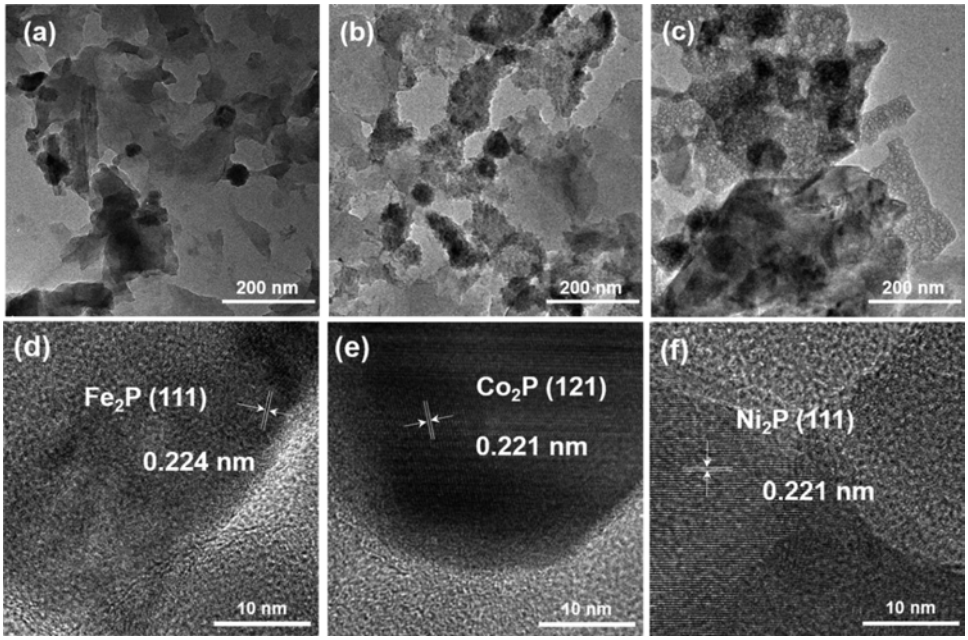

Fig. 2. TEM (a, b, and c) and HRTEM (d, e, and f) images of Fe_2P/S-CN (a and d), Co_2P/S-CN (b and e), and Ni_2P/S-CN (c and f).

hybrid. In addition, the components of Fe_2P, Co_2P, and Ni_2P were estimated by ICP (Table S1). The atomic ratios between Fe_2P, Co_2P, and Ni_2P are *ca.* 1.99, 2.02, and 2.00, respectively, which is in accord with the crystalline structure confirmed by XRD.

The TEM images are collected to characterize the morphologies and the structures of M_2P/S-CN. It is evident from Fig. S2 that as-prepared S-CN exists an amorphous structure with microscale layers. As present in Fig. 2a, it is found that Fe_2P with particle sizes around 30–50 nm were firmly anchored on the surface of S-CN to form a semiconductor-cocatalyst composites. To further accurately identify the crystal structure of Fe_2P on the surface of S-CN, the HRTEM measurements were performed. The lattice fringes with a d-spacing of 0.224 nm were observed (Fig. 2d), attributed to the (111) plane of hexagonal Fe_2P. In Co_2P/S-CN sample (Fig. 2b), small particles with ˜50 nm were observed and deposited on the surface of S-CN. The crystalline lattice spacing of 0.221 nm can be assigned to the (121) plane of orthorhombic Co_2P (Fig. 2e). In addition, Ni_2P/S-CN also shows the similar morphology to those of Fe_2P/S-CN and Co_2P/S-CN (Fig. 2c). Their corresponding HRTEM images are shown in Fig. 2f wherein the fringes with d spacing of 0.221 nm could be assigned to the (111) plane of Ni_2P. Therefore, the above results confirmed that the M_2P nanoparticles were successfully loaded on the surface of S-CN through an ultrasound assisted method in three M_2P/S-CN.

The energy dispersive X-ray (EDX) results clearly indicated the existence of C, N, S, P and metal in the selected region (Fig. S3), and no other element was detected except Cu (copper film). The corresponding EDX mapping results (Fig. 3) confirm the homogeneous distribution density of C and N, indicating the sheet-like morphology of S-CN. No obvious images belonging to sulfur were observed might result from the low content of sulfur in the as-prepared S-CN. The constituting elements metal and phosphide was well dispersed, with the same shape, further suggesting that M_2P still exists with the uniform distribution on the surface of S-CN after hybridization. Table S2 shows the BET of S-CN, Fe_2P/S-CN, Co_2P/S-CN, and Ni_2P/S-CN and the result indicates that all the samples exhibit the similar BET surface around 15 $m^2\,g^{-1}$.

To gain the information regarding the surface chemical compositions and valence state of S—CN, M_2P/S—CN and bulk M_2P, the XPS measurements were performed. As shown in Fig. S4, the XPS survey scan further verify that as-prepared M_2P/S—CN mainly consist of C, N, P, and corresponding metal element. The C 1 s XPS spectrum (Fig. 4a) proves the existences of the characteristic C-NH_2 and C═O species of S—CN [29], which are located at binding energies of 285.9 and 288.6 eV, respectively. The N 1 s XPS spectrum (Fig. 4b) reveals two peaks at 399.2 and 401.1 eV, corresponding to the characteristic sp^2-hybridized nitrogen involved in triazine rings (C–N = C) and free amino groups (C-*N*-H) from S—CN [30], respectively. After deposited the M_2P on the surface of S—CN, the binding energies of both C 1 s and N 1 s of M_2P/SCN shifted to higher values, demonstrating that the interaction between M_2P and S—CN [31]. The S 1 s XPS spectrum (Fig. 4c) certifies the existence of sulfur element and the weak intensity corresponds to the low content, in accordance with the EDS elemental mapping.

The local electronic structure of Fe 2p, Co 2p, Ni 2p, and P 2p in M_2P and M_2P/S-CN were further measured by XPS. As indicated in Fig. 5a, the XPS spectra of Fe $2p_{3/2}$ in bulk Fe_2P and Fe_2P/S-CN exists two peaks at around 706.7 and 710.9 eV to be originated from $Fe\delta^+$ and Fe^{2+} demonstrating the presence of Fe_2P [32–34]. Fig. 5b shows two peaks at 778.1 and 781.1 eV to be from elemental $Co\delta^+$ and Co^{2+} in the Co_2P cocatalysts [35,36]. For the Ni 2p region (Fig. 5c), two peaks at 853.3 and 856.2 eV were observed in Ni $2p_{3/2}$ window. The peak at 856.2 eV is attributed to Ni^{2+} due to surface oxidation in Ni_2P. The prominent peak at 853.3 eV is a little higher than that of metallic Ni (852.8 eV), indicating a slightly positive charge ($Ni\delta^+$) in Ni_2P [37]. From the P 2p peaks, two typical peaks at 130.1 and 129.4 eV are assigned to $P^{\delta-}$ species in metal phosphide [36]. A binding energy of 133.4 eV can be associated with phosphorous in phosphates [38,39]. Compared to pure M_2P, the binding energy of both metal 2p and P 2p of M_2P/SCN were slightly shifted to lower values (Fig. S5). It is concluded that, due to the high work function of M_2P, the introduction of M_2P into the surface of S-CN could give rise to a slight charge transfer from S-CN to M_2P [40].

The optical absorption of as-prepared g-C_3N_4, S-CN and M_2P/S-CN photocatalysts were measured by UV–vis diffuse reflectance spectroscopy (Fig. 6). The UV–vis spectra of pristine g-C_3N_4 and S-CN show the typical absorption edge at around 440 and 475 nm, respectively, confirming sulfur doping extends the absorption to the longer wavelength. The absorption edge of M_2P/S-CN has a slight change after M_2P loading, indicated that M_2P was deposited on the surface of S-CN. It is clear that M_2P/S-CN absorb more visible light than pristine S-CN, this may due to the black colour of M_2P. However, the physical properties of

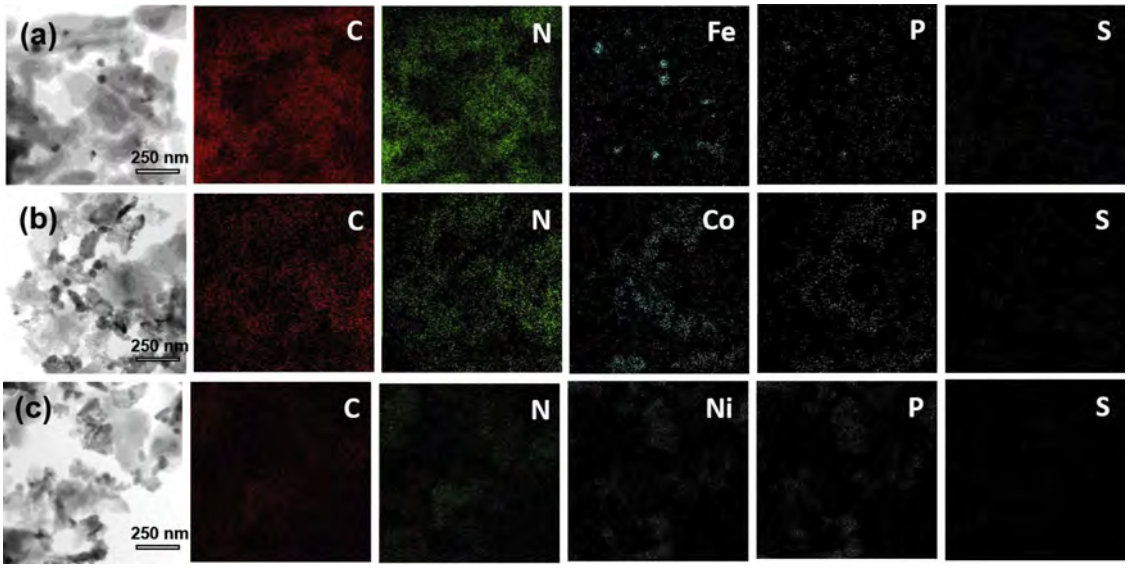

Fig. 3. EDX elemental mapping images for Fe_2P/S-CN (a), Co_2P/S-CN (b), and Ni_2P/S-CN (c).

the M_2P are similar to metallic nature rather than semiconductor [41], leading to a similar adsorption edge of M_2P/S-CN. This confirmed that the absorption of metal phosphide is impossible to produce excitation electron for further H_2 generation reaction [15,20], which means the difference between light absorption of S-CN and M_2P/S-CN is not the key point for the photocatalytic activity.

The performance of M_2P/S−CN, S−CN, and Pt/S−CN for photocatalytic H_2 generation was measured in a TEOA solution under four different band pass filters at $\lambda = 400$, 440, 480, or 520 nm, as demonstrated in Fig. 7. It can be seen that only a trace of H_2 was detected over bare S−CN after irradiation for 1 h at four wavelengths, suggesting the ultrafast recombination between photogenerated electron and hole in pristine S−CN. Notably, the yield of H_2 generation significantly increased after S−CN was hybridized with each type of M_2P, indicating that all three types of M_2P can be used as a cocatalyst for efficient H_2 generation by S−CN. For three as-prepared samples, the photocatalytic activity of H_2 generation decreased dramatically along with the increase of the wavelength, consistent with the UV–vis absorption spectrum of the corresponding M_2P/S−CN. The results demonstrated that M_2P work as an efficient cocatalyst rather than semiconductor to enhance the photocatalytic H_2 generation activity. Among three M_2P/S−CN, Ni_2P/S−CN showed the highest H_2 generation activity of 0.41 $\mu mol \cdot h^{-1}$ at $\lambda = 400$ nm, while Co_2P/S−CN had a comparable H_2 generation rate of 0.39 $\mu mol \cdot h^{-1}$ under the same condition, and Fe_2P/S−CN showed the smallest rate of 0.32 $\mu mol \cdot h^{-1}$. The H_2 generation rates of Ni_2P/S−CN, Co_2P/S−CN, and Fe_2P/S−CN are approximately 22.7, 21.4, and 17.9 times higher than that of S−CN, respectively. It is common knowledge that Pt is the most efficient cocatalyst for the H_2 generation activity. Thus, the photocatalytic H_2 generation activity of Pt/S−CN was measured to compare with M_2P/S−CN under the same condition and loading amount. The results show that the M_2P/S−CN exhibits the comparable H_2 generation rate with that of Pt/S−CN, demonstrating that M_2P is a good noble-metal-free cocatalyst when hybridized with S−CN.

Furthermore, the stability and reusability of M_2P/S-CN was evaluated by the cycling H_2 generation under a prolonged visible light irradiation of 9 h. As observed in Fig. S6, three M_2P/S-CN showed a constant H_2 production rate during each cycle and a negligible of activity loss was detected after three cycles, suggesting that three M_2P/S-CN are highly stable during the photocatalytic H_2 generation. In addition, the H_2 generation activity of Pt/S-CN, Fe_2P/S-CN, Co_2P/S-CN, Ni_2P/S-CN, and Pt/g-C_3N_4 under visible-light irradiation ($\lambda > 400$ nm) is shown in Fig. S7. Pt/S-CN has the extended absorption from 400 nm to 475 nm to show a higher photocatalytic activity compared to Pt/g-C_3N_4 (0.64 vs 0.53 $\mu mol \cdot h^{-1}$). The H_2 generation activity of M_2P/S-CN is in the order of Ni_2P/S-CN, Co_2P/S-CN, and Fe_2P/S-CN, to be higher than that of Pt/g-C_3N_4.

The PL spectra were measured to discuss on the charge separation performance in the excited semiconductors [36]. Here, the PL spectra of S-CN and M_2P/S-CN were measured to study the key role of M_2P in determining the enhanced photocatalytic activity. As shown in Fig. 8a, when the excitation wavelength was at 385 nm, a broad emission peak centered at ca. 460 nm was observed for S-CN and M_2P/S-CN. It is observed that the emission intensity of the pure S-CN is the strongest, corresponding to the charge recombination in the S-CN. However, after the M_2P loading on the surface of S-CN, the intensity of this emission

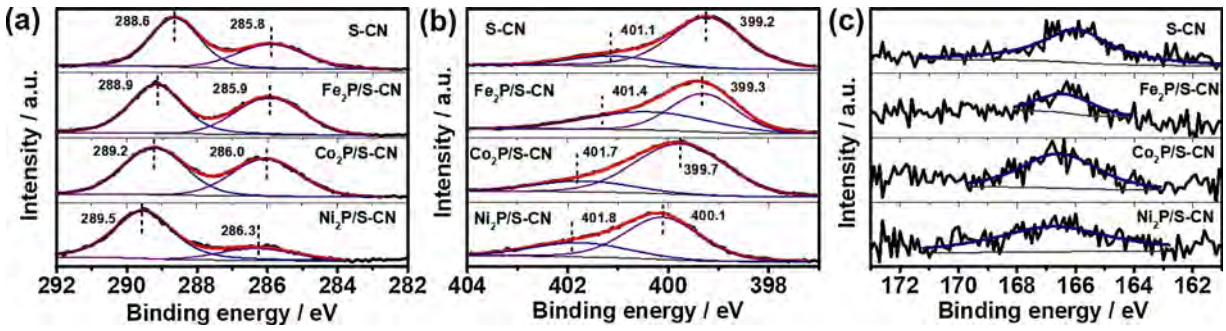

Fig. 4. XPS spectra of C 1 s (a), N 1 s (b), and S 1 s (c) of S-CN, Fe_2P/S-CN, Co_2P/S-CN, and Ni_2P/S-CN.

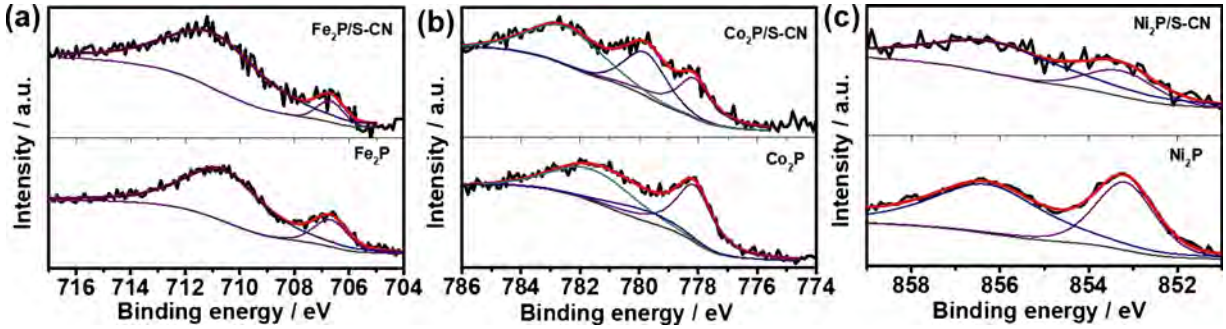

Fig. 5. XPS spectra of Fe 2p (a) of Fe_2P and Fe_2P/S-CN; Co 2p (b) of Co_2P and Co_2P/S-CN; and Ni 2p (c) of Ni_2P and Ni_2P/S-CN.

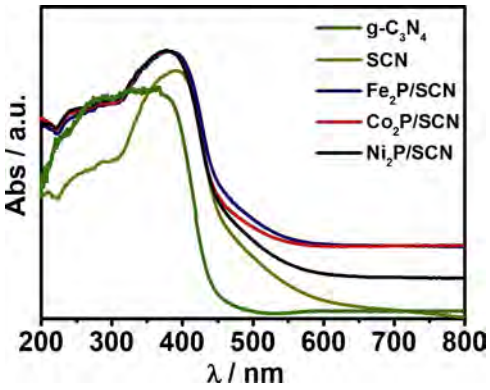

Fig. 6. UV–vis DRS of g-C_3N_4, S-CN, Fe_2P/S-CN, Co_2P/S-CN, and Ni_2P/S-CN.

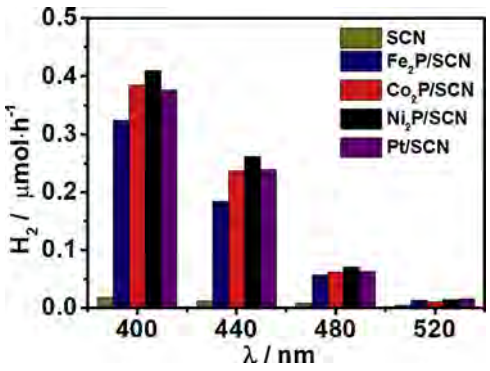

Fig. 7. Photocatalytic H_2 generation rates for S-CN, Fe_2P/S-CN, Co_2P/S-CN, Ni_2P/S-CN, and Pt/S-CN.

peak dropped significantly, suggesting that the efficient inhibition of photogenerated electron-hole pairs recombination is achieved in M_2P/S-CN. The PL intensities decreased in the order of Ni_2P/S-CN > Co_2P/S-CN > Fe_2P/S-CN, consistent with that of the photocatalytic H_2 generation activity. Thus, the electron transfer quenching of excited S-CN by M_2P is the key for efficient photocatalytic H_2 generation. To understand the photophysical behaviours of photoexcited charge carriers, the time-resolved fluorescence decay spectra of the S-CN, Fe_2P/S-CN, Co_2P/S-CN, Ni_2P/S-CN, and Pt/S-CN were recorded. Fig. 8b shows the representative time-resolved fluorescence decays curves after pulsed excitation at λ = 420 nm. Fitting the decay spectrum shows three radiative lifetimes are 2.82, 2.45, 2.10, 1.83, and 1.57 ns for S-CN, Fe_2P/S-CN, Pt/S-CN, Co_2P/S-CN, and Ni_2P/S-CN, respectively, showing that the lifetime decreases on introducing cocatalysts. This indicates that the transfer of photoexcited electrons and holes between S-CN and cocatalysts must exist, which can retard the recombination probability of electron and hole pairs and thus improve its photoactivity. The decreased emission lifetime of M_2P/g-C_3N_4 signifies the rapid interfacial electron injection from g-C_3N_4 to M_2P, which are in accordance with the PL quenching measurements.

The efficiency of charge separation and transfer was further verified by the photocurrent, electrochemical impedance spectroscopy (EIS), and polarization curves, as shown in Fig. S8. Photocurrent responses are usually used to evaluate the visible light photoelectrochemical performance occurring on the photocatalyst surface [42]. Fig. S8a shows the several cycles of switch-on/off under visible light irradiation (λ > 420 nm). In each cycle, the photocurrent intensity showed a quick increase when the light was switched on and decay to baseline as soon as turned off. The pristine S-CN exhibits rather low photocurrent intensity, while those of M_2P/S-CN were obviously enhanced under the same condition. Therefore, it is concluded that M_2P/S-CN had lower recombination rate and a more efficient charge separation and charge transfer, leading to the efficient photocatalytic H_2 generation activities.

The photocurrent intensity decreased in the order of Ni_2P/S-

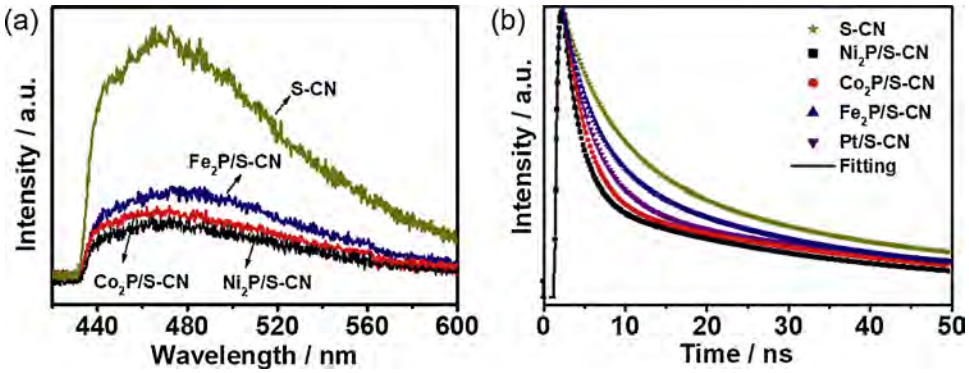

Fig. 8. (a) PL spectra of S-CN, Fe_2P/S-CN, Co_2P/S-CN, and Ni_2P/S-CN. (b) Time-resolved fluorescence decay curves (excitation: λ = 420 nm) for S-CN, Fe_2P/S-CN, Co_2P/S-CN, Ni_2P/S-CN and Pt/S-CN.

CN > Co_2P/S-CN > Fe_2P/S-CN. EIS Nyquist plots of S-CN and M_2P/S-CN were tested, as another effective measurement to clear the different property of cocatalysts in charge transfer and separation process (Fig. S8b). The smallest diameter was observed for Ni_2P/S-CN, followed by Co_2P/S-CN, Fe_2P/S-CN, and S-CN, suggesting that M_2P accelerate remarkably the charge transfer and separation of S-CN. In other words, M_2P cocatalyst could lead to the accelerated charge transfer resistance for dominantly improving the H_2 generation. Additionally, the polarization curves of S-CN and M_2P/S-CN were measured ranging from −0.4 to −1.2 V versus Ag/AgCl, corresponding to the reduction of water to H_2. As shown in the Fig. S8c, M_2P/S-CN shows stronger reduction current peak than that of S-CN and in the order of Ni_2P/S-CN > Co_2P/S-CN > Fe_2P/S-CN. Much more pronounced cathodic current density and low overpotential over M_2P/S-CN demonstrate that electron migration rate increases to result in the efficient photocatalytic activity [36]. These results further confirm the enhanced charge transfer and recombination inhibition over M_2P/S-CN.

As mentioned above, Ni_2P/S-CN showed the highest photocatalytic H_2 generation activity. To unveil the synergistic nature among these cocatalysts, DFT calculations were performed to compare the intermediate H* adsorption free energies (ΔG_H) of the several models including S-CN, Fe_2P/S-CN, Co_2P/S-CN and Ni_2P/S-CN. The computational details can be obtained in the Supporting Information. The whole reaction process mainly consists of proton adsorption and reduction on the catalyst, followed by desorption of the hydrogen molecular. In this respect, two possible reaction mechanisms are widely accepted, namely Volmer-Tafel and Volmer-Heyrovsky [43]. Theoretically, for an ideal catalyst for photocatalytic H_2 generation, the absolute value of ΔG_H should be close to 0, which is favorable for the H* adsorption and subsequent desorption, thus promoting the H_2 production [44]. Fig. 9a shows the H* adsorption free energies on various catalysts. Obviously, the H* adsorption on pristine S-CN was too strong, implying the low catalytic activity due to the high overpotential and possible sluggish H_2 desorption process. Strikingly, after the deposition of M_2P, the overpotential was distinctly decreased from –0.93 to –0.38, –0.29 and –0.24 eV for Fe_2P/S-CN, Co_2P/S-CN and Ni_2P/S-CN, respectively. Therefore, Ni_2P/S-CN showed the highest photocatalytic H_2 generation activity among these four models, confirming the experimentally observed H_2 generation rates. In addition, to further clarify the promoting mechanism of Ni_2P/S-CN, the charge transfer was explored as shown in Fig. 9b. The formation of interface induces a vigorous charge transfer from S-CN to Ni_2P, thus increasing the local electron density of Ni_2P, benefiting surface hydrogen generation and catalytic activity [45]. Thus, the overpotential can be effectively tuned through the engineering of M_2P cocatalysts, thereby improving the catalytic performance of M_2P/S-CN.

Base on the above results, a possible photocatalytic mechanism is depicted in Scheme 1. When M_2P/S−CN were irradiated at the effective wavelength, S−CN absorbs photons to generate electrons and holes, then the electron could be excited from valence band (VB) of S−CN to its conduction band (CB). M_2P, with their metallic nature, provides no extra absorption capacity, but serve the role of an electron acceptors to accept photo-induced electron during the process of photocatalytic reaction. On the other hand, the oxidation of TEOA, as a sacrificial agent, could consume the redundant photogenerated holes in the VB of S−CN. Thus, M_2P could suppresses the recombination of electron-hole pairs in S−CN, lead to the efficient photocatalytic H_2 generation.

By comparison of three M_2P, Fe_2P and Ni_2P have the same crystal structure belonging to hexagonal, whereas Co_2P has an orthorhombic one [46,47]. In contrast, the photocatalytic H_2 generation activity of M_2P/S-CN is in the order of Fe_2P/S-CN < Co_2P/S-CN < Ni_2P/S-CN, suggesting that the crystal structure of M_2P is not dominant factor for the photocatalytic H_2 generation activity of M_2P/S-CN. The PL spectra, fluorescence decay and photoelectrochemical characterization suggest that the high H_2 generation activity corresponds to the efficient electron transfer from S-CN to M_2P, and this can be further confirmed by the highest binding energy for the C and N XPS peaks of Ni_2P/S-CN than for Co_2P/S-CN, Fe_2P/S-CN, and S-CN, as shown in Fig. 4 [40]. Meanwhile, the intermediate H* adsorption free energies of M_2P/ S-CN, as other reason is also performed by DFT calculations. In another words, Ni_2P/S-CN with the lowest overpotential exhibits the highest efficiency for electron transfer from S-CN to Ni_2P, suggesting that Ni_2P could be worked as a better H^+ acceptor to facilitate the reduction of H^+ to H_2 [48]. Thus, it can be concluded that Ni_2P are working as an efficient cocatalyst to accept the photo-induced electron in the CB of S-CN, leading to the reduction of H^+ to generate H_2.

4. Conclusions

Three types of M_2P (M = Fe, Co, and Ni) hybridized on S-CN have been synthesized via an ultrasound assisted method. Three as-prepared M_2P can serve as an efficient non-noble metal cocatalyst for improving H_2 generation on S-CN. DFT calculations, PL spectra, photocurrent, and EIS studies revealed that the efficient H_2 generation activity mainly attribute to the lowest overpotential and efficient charge transfer from photoinduced S-CN to M_2P, which suppress the recombination of electron-hole pairs in S-CN. Among M_2P/S-CN, Ni_2P/S-CN exhibits the most efficient electron transfer ability from S-CN to Ni_2P, leading the highest photocatalytic H_2 generation activity. It is believed that electron transfer ability rather than crystal structure is the critical to effect on the photocatalytic activity. This current work add the importance of the interfacial charge transfer for three M_2P-S-CN photocatalytic activity and an opportunity to construct the low-cost, highly efficient solar energy conversion composites.

Acknowledgements

This work has been supported by Natural Science Foundation of China (21603024, 21577013, U1508205, and21373037), International S&T Cooperation Program of China (2016YFE0109800), the Liaoning

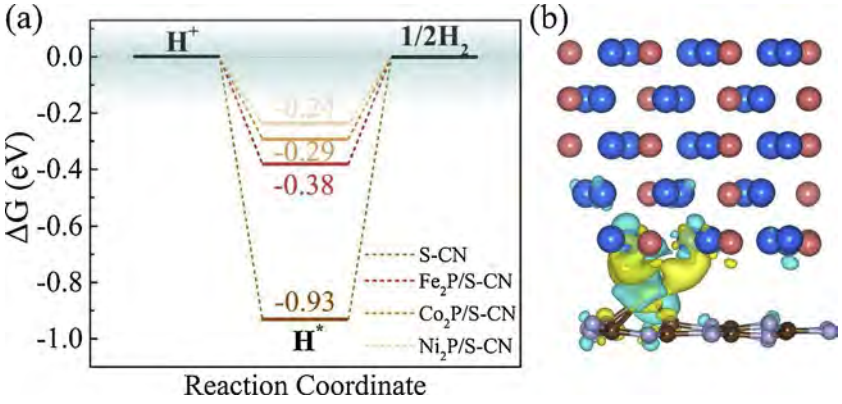

Fig. 9. (a) The free-energy diagram of the photocatalytic H_2 generation on S-CN, Fe_2P/S-CN, Co_2P/S-CN and Ni_2P/S-CN. (b) The charge density distributions of Ni_2P/S-CN system. Blue and yellow colors show the charge losing and gaining, respectively (For interpretation of the references to colour in this figure legend, the reader is referred to the web version of this article).

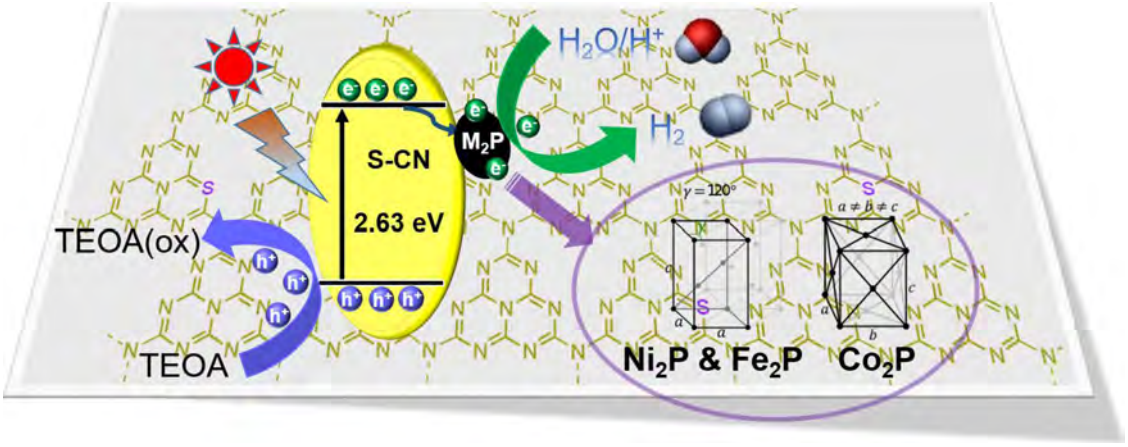

Scheme 1. Schematic illustration of the photocatalytic H_2 generation for M_2P/S-CN.

Province Doctor Startup Fund (201601038), and the Fundamental Research Funds for the Central Universities (DUT16ZD224), and a Grant-in-Aid for Scientific Research (project 25220806 and others) from the Ministry of Education, Culture, Sports, Science and Technology (MEXT) of the Japanese Government.

Appendix A. Supplementary data

Supplementary material related to this article can be found, in the online version, at doi:https://doi.org/10.1016/j.apcatb.2019.01.072.

References

[1] G.J. Hughes, A. Mckinley, R.H. Williams, J. Phys. C: Solid State Phys. 16 (1983) 2391–2406.
[2] S.T. Oyama, J. Catal. 216 (2003) 343–352.
[3] W.R.A.M. Robinson, J.N.M. vanGestel, T.I. Koranyi, S. Eijsbouts, A.M. vanderKraan, J.A.R. vanVeen, V.H.J. deBeer, J. Catal. 161 (1996) 539–550.
[4] J.F. Callejas, C.G. Read, C.W. Roske, N.S. Lewis, R.E. Schaak, Chem. Mater. 28 (2016) 6017–6044.
[5] S. Boyanov, K. Annou, C. Villevieille, M. Pelosi, D. Zitoun, L. Monconduit, Ionics 14 (2008) 183–190.
[6] Y.M. Shi, B. Zhang, Chem. Soc. Rev. 45 (2016) 1529–1541.
[7] P. Liu, J.A. Rodriguez, J. Am. Chem. Soc. 127 (2005) 14871–14878.
[8] E.J. Popczun, J.R. McKone, C.G. Read, A.J. Biacchi, A.M. Wiltrout, N.S. Lewis, R.E. Schaak, J. Am. Chem. Soc. 135 (2013) 9267–9270.
[9] H. Zhao, Z.Y. Yuan, Catal. Sci. Technol. 7 (2017) 330–347.
[10] J.R. Ran, J. Zhang, J.G. Yu, M. Jaroniecc, S.Z. Qiao, Chem. Soc. Rev. 43 (2014) 7787–7812.
[11] B. Tian, Z. Li, W.L. Zhen, G.X. Lu, J. Phys. Chem. C 120 (2016) 6409–6415.
[12] P.F. Wang, T.F. Wu, C. Wang, J. Hou, J. Qian, Y.H. Ao, ACS Sustain. Chem. Eng. 5 (2017) 7670–7677.
[13] Z.J. Sun, H.L. Chen, Q. Huang, P.W. Du, Catal. Sci. Technol. 5 (2015) 4964–4967.
[14] Z.Y. Zhao, F. Tian, Acta Phys.-Chim. Sin. 32 (2016) 2511–2517.
[15] Z.J. Sun, H.F. Zheng, J.S. Li, P.W. Du, Energy Environ. Sci. 8 (2015) 2668–2676.
[16] J.Q. Tian, N.Y. Cheng, Q. Liu, W. Xing, X.P. Sun, Angew. Chem. Int. Ed. 54 (2015) 5493–5497.
[17] Z.J. Sun, B.H. Lv, J.S. Li, M. Xiao, X.Y. Wang, P.W. Du, J. Mater. Chem. A 4 (2016) 1598–1602.
[18] S.S. Yi, J.M. Yan, B.R. Wulan, S.J. Li, K.H. Liu, Q. Jiang, Appl. Catal. B 200 (2017) 477–483.
[19] W.Z. Gao, Y. Xu, Y. Chen, W.F. Fu, Chem. Commun. 51 (2015) 13217–13220.
[20] A. Indra, A. Acharjya, P.W. Menezes, C. Merschjann, D. Hollmann, M. Schwarze, M. Aktas, A. Friedrich, S. Lochbrunner, A. Thomas, M. Driess, Angew. Chem. Int. Ed. 56 (2017) 1653–1657.
[21] Y. Pan, Y. Lin, Y.J. Chen, Y.Q. Liu, C.G. Liu, J. Mater. Chem. A 4 (2016) 4745–4754.
[22] Z.C. Sun, M.S. Zhu, M. Fujitsuka, A.J. Wang, C. Shi, T. Majima, ACS Appl. Mater. Interfaces 9 (2017) 30583–30590.
[23] P. Liu, J.A. Rodriguez, J. Am. Chem. Soc. 127 (2005) 14871–14878.
[24] Z.F. Hu, Z.R. Shen, J.C. Yu, Green Chem. 19 (2017) 588–613.
[25] A.E. Henkes, Y. Vasquez, R.E. Schaak, J. Am. Chem. Soc. 129 (2007) 1896–1897.
[26] X.Q. Wang, P. Clark, S.T. Oyama, J. Catal. 208 (2002) 321–331.
[27] A.J. Wang, M.L. Qin, J. Guan, L. Wang, H.C. Guo, X. Li, Y. Wang, R. Prins, Y.K. Hu, Angew. Chem. Int. Ed. 47 (2008) 6052–6054.
[28] K. Wang, Q. Li, B. Liu, B. Cheng, W. Ho, J. Yu, Appl. Catal. B 176-177 (2015) 44–52.
[29] J.C. Wang, C.X. Cui, Y. Li, L. Liu, Y.P. Zhang, W.N. Shi, J. Hazard. Mater. 339 (2017) 43–53.
[30] Q.Y. Lin, L. Li, S.J. Liang, M.H. Liu, J.H. Bi, L. Wu, Appl. Catal. B 163 (2015) 135–142.
[31] J.Q. Yan, H. Wu, H. Chen, L.Q. Pang, Y.X. Zhang, R.B. Jiang, L.D. Li, S.Z. Liu, Appl. Catal. B 194 (2016) 74–83.
[32] F. Luo, H.L. Su, W. Song, Z.M. Wang, Z.G. Yan, C.H. Yan, J. Mater. Chem. 14 (2004) 111–115.
[33] F.L. Wang, H.G. Xue, Z.Q. Tian, W. Xing, L.G. Feng, J. Power Sour. 375 (2018) 37–42.
[34] L. Kong, J. Yan, P. Li, S.F. Liu, ACS Sustain. Chem. Eng. 6 (2018) 10436–10444.
[35] H.W. Hou, Q. Peng, S.Y. Zhang, Q.X. Guo, Y. Xie, Eur. J. Inorg. Chem. 13 (2005) 2625–2630.
[36] K.L. Yan, X. Shang, L.M. Zhang, B. Dong, Z.Z. Liu, J.Q. Chi, W.K. Gao, Y.M. Chai, C.G. Liu, Electrochim. Acta 249 (2017) 16–25.
[37] H.M. Chen, J.J. Tan, Y.L. Zhu, Y.W. Li, Catal. Commun. 73 (2016) 46–49.
[38] C.H. An, Y.J. Wang, Y.P. Wang, G. Liu, L. Li, F.Y. Qiu, Y.A. Xu, L.F. Jiao, H.T. Yuan, RSC Adv. 3 (2013) 4628–4633.
[39] L. Kong, Y. Ji, Z. Dang, J. Yan, P. Li, Y. Li, S.F. Liu, Adv. Funct. Mater. 28 (2018) 1800668.
[40] G.G. Liu, P. Li, G.X. Zhao, X. Wang, J.T. Kong, H.M. Liu, H.B. Zhang, K. Chang, X.G. Meng, T. Kako, J.H. Ye, J. Am. Chem. Soc. 138 (2016) 9128–9136.
[41] S.T. Oyama, T. Gott, H. Zhao, Y.-K. Lee, Cataly. Today 143 (2009) 94–107.
[42] J.Q. Wen, J. Xie, H.D. Zhang, A.P. Zhang, Y.J. Liu, X.B. Chen, X. Li, ACS Appl. Mater. Interfaces 9 (2017) 14031–14042.
[43] J. Kibsgaard, C. Tsai, K. Chan, J.D. Benck, J.K. Norskov, F. Abild-Pedersen, T.F. Jaramillo, Energy Environ. Sci. 8 (2015) 3022–3029.
[44] J.K. Norskov, T. Bligaard, A. Logadottir, J.R. Kitchin, J.G. Chen, S. Pandelov, J.K. Norskov, J. Electrochem. Soc. 152 (2005) J23–J26.
[45] Z.C. Zhuang, Y. Li, Z.L. Li, F. Lv, Z.Q. Lang, K.N. Zhao, L. Zhou, L. Moskaleva, S.J. Guo, L.Q. Mai, Angew. Chem. Int. Ed. 57 (2018) 496–500.
[46] R. Fruchart, A. Roger, J.P. Senateur, J. Appl. Phys. 40 (1969) 1250–1257.
[47] P.E.R. Blanchard, A.P. Grosvenor, R.G. Cavell, A. Mar, Chem. Mater. 20 (2008) 7081–7088.
[48] C.Y. Jiang, X.X. Xu, M.L. Mei, F.N. Shi, ACS Sustain. Chem. Eng. 6 (2018) 854–861.